Probabilistic Moment Tensor Inversion for Hydrocarbon-Induced Seismicity in the Groningen Gas Field, the Netherlands, Part 2: Application

Bernard Dost*[1], Annemijn van Stiphout[2], Daniela Kühn[3], Marloes Kortekaas[4], Elmer Ruigrok[1], and Sebastian Heimann[5]

ABSTRACT

Recent developments in the densification of the seismic network covering the Groningen gas field allow a more detailed study of the connection between induced seismicity and reactivated faults around the gas reservoir at 3 km depth. With the reduction of the average station distance from 20 km to 4–5 km, a probabilistic full-waveform moment tensor inversion procedure could be applied, resulting in both improved hypocenter location accuracy and full moment tensor solutions for events of $M \geq 2.0$ recorded in the period 2016–2019. Hypocenter locations as output from the moment tensor inversion are compared to locations from the application of other methods and are found similar within 250 m distance. Moment tensor results show that the double-couple (DC) solutions are in accordance with the known structure, namely normal faulting along 50°–70° dipping faults. Comparison with reprocessed 3D seismic sections, extended to a depth of 6–7 km, demonstrate that (a) most events occur along faults with a small throw and (b) reactivated faults in the reservoir often continue downward in the Carboniferous underburden. From non-DC contributions, the isotropic (ISO) component is dominant and shows consistent negative values, which is expected in a compacting medium. There is some indication that events connected to faults with a large throw (>70 m) exhibit the largest ISO component (40%–50%).

KEY POINTS

- We apply a probabilistic full moment tensor inversion to induced seismicity in the Groningen gas field.
- Reactivated faults are identified, and a consistently negative isotropic component was found (up to 50%).
- Source mechanisms of induced events allow identification of reactivated faults.

Supplemental Material

INTRODUCTION

The Groningen field in the northeast of the Netherlands is one of the largest on-shore gas fields in the world and is in production since 1963. There is no known natural seismicity in the region. Induced seismicity in the field started in 1991 and shows an increase in activity and magnitude with time. The field is produced by the Nederlandse Aardolie Maatschappij (NAM). Bourne *et al.* (2014) show that the occurrence of seismicity in space and time correlates well with the development of compaction at reservoir level. Although it is assumed that seismicity occurs along reactivated faults in the reservoir, until recently a proper connection between known faults and induced seismicity could not be made due to limited resolution of event hypocenters and source mechanisms (e.g., Dost and Haak, 2007). Limited hypocenter resolution was caused by the sparse monitoring network, designed to cover a larger region including Groningen and characterized by an average interstation spacing of 20 km as well as the use of an average 1D velocity model, smoothing lateral variations in shallow crustal structure in the north of the Netherlands, mainly due to salt tectonics. Since the end of 2015, a new dense borehole

1. Royal Netherlands Meteorological Institute (KNMI), De Bilt, The Netherlands; 2. Utrecht University, Utrecht, The Netherlands; 3. NORSAR, Kjeller, Norway; 4. Energie Beheer Nederland (EBN B.V.), Utrecht, The Netherlands; 5. German Research Center for Geosciences, Physics of Earthquakes and Volcanoes (GFZ), Potsdam, Germany

*Corresponding author: bernard.dost@knmi.nl

Cite this article as Dost, B., A. van Stiphout, D. Kühn, M. Kortekaas, E. Ruigrok, and S. Heimann (2020). Probabilistic Moment Tensor Inversion for Hydrocarbon-Induced Seismicity in the Groningen Gas Field, the Netherlands, Part 2: Application, *Bull. Seismol. Soc. Am.* **110**, 2112–2123, doi: 10.1785/0120200076

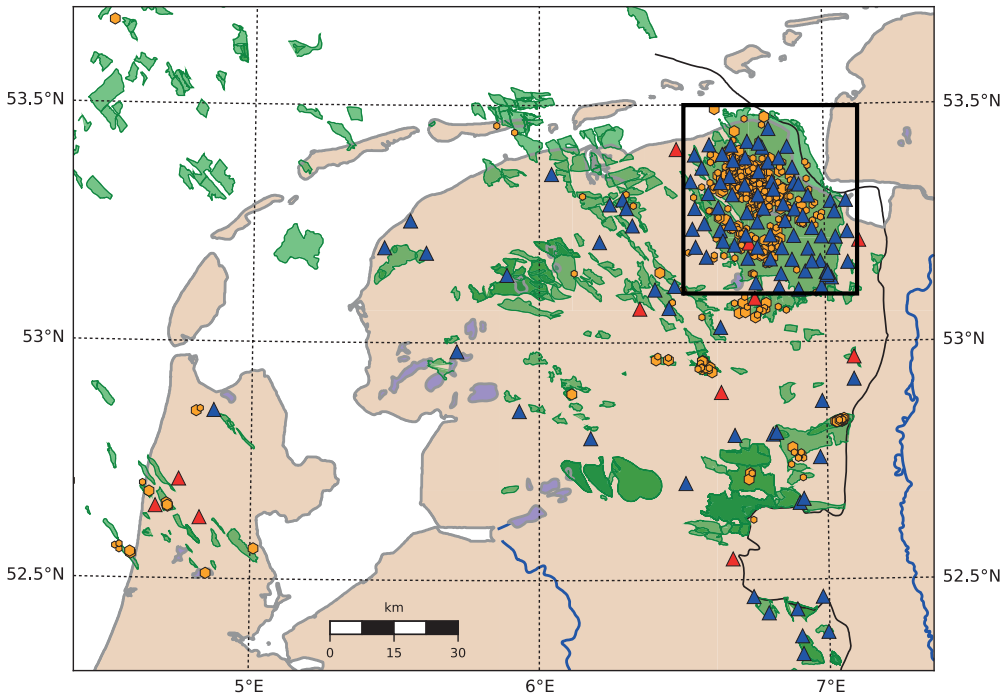

Figure 1. Location of the Groningen gas field (inside the black square) in the north of the Netherlands. The borehole network is shown as blue triangles. The original borehole network installed in 1995 is shown as red triangles. Gas fields are shown as green polygons and rivers and lakes in blue. Induced seismicity in the north of the Netherlands (1986–2020) is shown as orange circles.

geophone network is operational, covering the Groningen gas field (Fig. 1, for details see Dost *et al.*, 2017), designed to overcome the limitations of the old network. In addition, a 3D velocity model for both P and S waves is available for the Groningen region (Romijn, 2017). Both developments allowed to apply new techniques to improve the accuracy of hypocenter locations (Li *et al.*, 2016; Spetzler and Dost, 2017; Willacy *et al.*, 2018, 2019). By default, the depth of induced events was fixed at 3 km, the average depth of the reservoir, during the hypocenter inversion. The validity of this assumption was confirmed by Pickering (2015), who analyzed geophone data from two deep boreholes at reservoir level in the central part of the Groningen field and concluded that all events occurred at reservoir depth (2.8–3.0 km). This was further confirmed in a later study by Daniel *et al.* (2016), using the same deep boreholes.

Spetzler and Dost (2017) employed data from the shallow boreholes of the new network and an adaptation of the equal differential time (EDT) method (Lomax, 2005) to determine more accurate locations in the field. In their procedures a local 1D model, derived from the 3D model, was used and travel times were calculated. Willacy *et al.* (2018, 2019) studied the same region using a full-waveform modeling approach and concluded that relying on a 1D invariant model and single arrival travel times was not sufficient for Groningen. In a follow-up on the original article, Spetzler and Dost (in preparation) implemented a fast 3D raytracer in the EDT method and obtained comparable results to Willacy *et al.* (2019). Epicentral location accuracy in both studies is around 100–200 m, and results show a high correlation between relocated hypocenters and existing faults in the reservoir. The geometry of these faults is well known from high-resolution 3D seismic data (Kortekaas and Jaarsma, 2017).

The new network also allows for a moment tensor inversion, the next step in connecting existing faults to observed seismicity. Kraaijpoel and Dost (2013) show first results of source mechanisms for Groningen, based on inversion of polarization data and amplitude ratios and solving for a double-couple (DC) mechanism. Mainly normal-faulting mechanisms were found, in line with what is expected from the geological model (NAM, 2016), but the resolution of the solutions was limited. Willacy *et al.* (2018) processed all events of $M_L > 1.0$ in the region for the period January 2015 to September 2017. They conclude that the locations show a very good correlation with major faults in the reservoir, and that the DC component of the source mechanism is, in general, consistent with normal faulting. They found the largest source of error in the earthquake location in the vertical depth accuracy. In a follow-up of this article, Willacy *et al.* (2019) explain the methods in more detail and show results for events in the same time period for events of $M_L > 0$. The finite-difference modeling applied in this study is computationally intensive. As an alternative, we apply a full-waveform probabilistic optimization method, implemented in the Grond software, as part of the Pyrocko package (Heimann *et al.*, 2017). This probabilistic implementation yields insights in uncertainties and parameter trade-offs (Kühn *et al.*, 2020). We use locally averaged 1D velocity models, derived from the 3D velocity model for Groningen. For a given reference location, the mean interface depth and layer velocity at the interface depth are calculated for a box, centered at the reference location, with 5 km ribs. This averaging is based on data from the 3D model. Using depth-dependent relations for V_P and V_S in Romijn (2017), velocities are calculated for the 1D model.

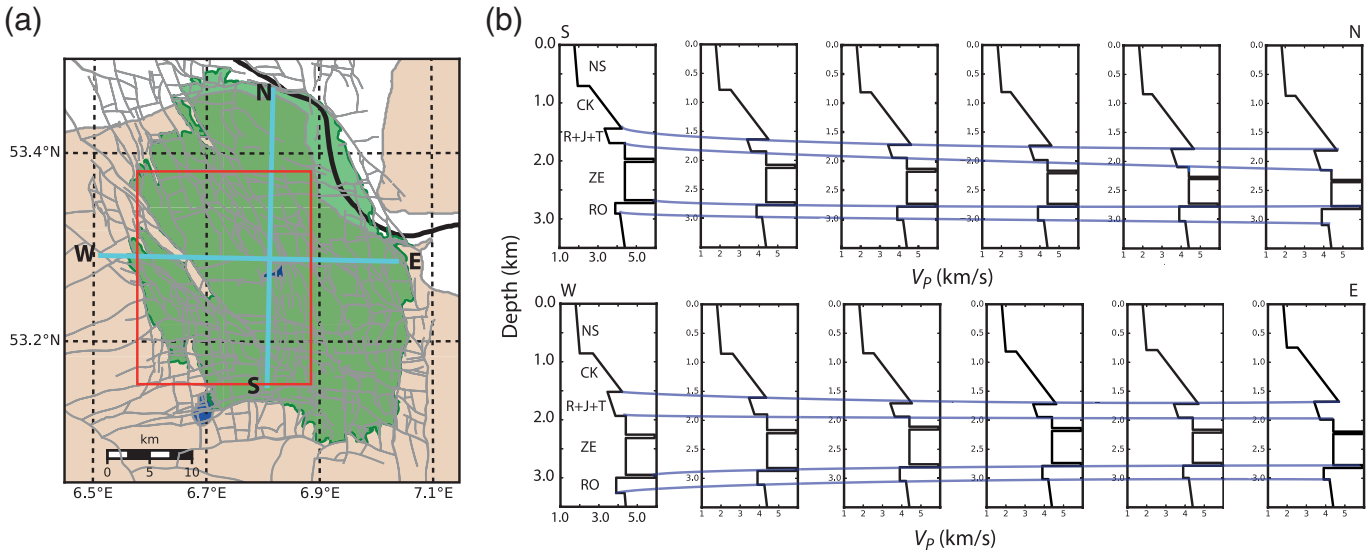

Figure 2. An east–west (E-W) and north–south (N-S) transect through the Groningen field, shown as a green polygon (a), displaying model-averaged P-wave velocity values and average depths of the interfaces (b). Model values are averaged over a box with a 5 km radius. CK, Chalk formation; NS, North Sea formation; R + J + T = Rijnland, Jurassic, and Triassic formations; RO, Rotliegend reservoir; ZE, Zechstein. The continuation of selected interfaces over the gas field is indicated with light blue lines in (b). Gray lines indicate faults at RO level. The red box in panel (a) indicates the position of the selected area in Figure 4.

In the present article, we investigate locations and moment tensor solutions for events in the Groningen region for the period January 2016 to July 2019. A description of the moment tensor inversion method and thorough testing of input parameters for the Groningen network can be found in Kühn *et al.* (2020).

Moment tensor inversions for induced seismicity often report the existence of non-DC components (e.g., McGarr, 1992; Fletcher and McGarr, 2005; Julià *et al.*, 2009; Kühn and Vavryčuk, 2013; Pesicek *et al.*, 2016; Zhang *et al.*, 2016; Martínez-Garzón *et al.*, 2017; Wang *et al.*, 2018). Therefore, it was decided to invert for the full moment tensor and evaluate the effect of possible volume changes, through the isotropic (ISO) component, as well as contributions of compensated linear vector dipole (CLVD) components. Furthermore, we will compare results of the moment tensor inversion with known aspects of existing faults determined from seismic reflection data, as dip direction and fault throw.

MOMENT TENSOR INVERSION

The new dense borehole network in Groningen consists of 200 m deep boreholes with three-component 4.5 Hz geophones at 50 m spacing. In addition, an accelerometer is added at the surface. The boreholes are uncased, so the orientation of instruments at installation is unknown. The orientations of the sensors at depth were determined using correlations with surface sensors (Hofman *et al.*, 2017), check-shots within 1 km distance from the stations, local events, and known explosions in the region (Ruigrok *et al.*, 2019). For the inversion, we focus on the lower sensor levels at 150 and 200 m depth, because background noise is lowest. Another reason is that the top 50 m in Groningen show large velocity contrasts (Noorlandt *et al.*, 2018) that are not incorporated in the velocity model. When using the deeper geophone levels, complexities from the near surface can be omitted from the misfit functions.

The geological structure of the Groningen gas field is well known (e.g., de Jager and Visser, 2017). Figure 2 shows two *P*-wave velocity profiles through the Groningen field, based on imaging of seismic data collected by the industry in 2015–2016 (Romijn, 2017). The top of the reservoir is situated at depths between 2.6 km in the south and 3.0 km in the north, and is marked with Rotliegend (RO). The thickness of the reservoir varies between 150 m in the south to 300 m in the north of the field. The reservoir is overlain by a Zechstein (ZE) salt layer in which thin (50–100 m) anhydrite layers are present and visible in Figure 2 as high-velocity layers. Between the base of the Chalk formation (CK) and top ZE three formations (Rijnland, Jurassic, and Triassic formations; R+J+T) are combined in the 2017 version of the 3D velocity model (Romijn, 2017). On top of the CK the North Sea (NS) formation is situated. In general, we observe an increase in the depth of the base of the chalk from south to north and, less pronounced, a deepening of the top reservoir. From west to east, the opposite is true: a shallowing of the top of the reservoir is observed. These averaged models show a smooth transition over the field. However, in locations where a salt dome is present, mainly at the edges of the field, the lateral variations in velocity increase, and this results in a large uncertainty in the average depth of the interfaces. Fortunately, also an *S*-wave model is available for the region, based on a limited number of sonic logs from

deep wells. Especially important is the fact that the upper NS formation (0–300 m) shows a depth-dependent V_P/V_S ratio. The velocity of the Carboniferous strata below the reservoir is much less known. The upper part of the Carboniferous underburden is characterized by a positive velocity gradient. The lower Carboniferous has significantly higher V_P due to the presence of a Dinantian carbonate platform. The top of this platform varies below Groningen between about 4.5 and 7 km depth (Kortekaas and Jaarsma, 2017).

We used a full-waveform probabilistic optimization method (Grond, see Data and Resources, Heimann *et al.*, 2017) for the moment tensor inversions and event locations, and local average 1D models derived from the 3D velocity model for Groningen (Romijn, 2017). Green's functions are calculated using an orthonormal propagator method that Wang (1999) implemented in the QSEIS program (see Data and Resources). For the calculation of the Green's functions, a source depth between 2.6 and 3.2 km was selected, as well as a distance range between 0 and 15 km with a 50 m spacing and a sampling rate of 25 Hz. The distance range is limited, because we focus on the direct *P* and *S* waves in the inversion. Because of the high-velocity anhydrite and salt layer on top of the reservoir, a significant defocusing effect is generated, enlarging the epicentral distance range to approximately 8 km, despite the very shallow depth of the sources (Kraaijpoel and Dost, 2013). Comparable methods have recently been developed by Gu *et al.* (2018) and Tan *et al.* (2018). However, there are important differences in the way the parameter space is searched. Our approach is more data-driven and flexible, in comparison with the method of Gu *et al.* (2018), whereas compared to the method by Tan *et al.* (2018), our approach has a more integrated way of assessing uncertainties. Details of these comparisons can be found in Kühn *et al.* (2020).

In the inversion procedure decisions should be made on parameters like the length of the time window around the *P* and *S* waves, which components to select, the frequency range used, and the number of iterations sampling the model space. For induced seismicity in Groningen, Kühn *et al.* (2020) carried out extensive testing of these parameters and suggested optimal values, which we followed. Therefore, the vertical and transverse components were used in the inversion. Addition of the radial component did not make a significant change in location and moment tensor solution, and this restriction reduced the computation time. In general, we followed the recommendation of a time window over the *P* and *S* waves of 0.5 s, but, for some events, a window up to 1 s has been applied to the *P* onset. The frequency range applied in the inversion was limited to 1–4 Hz. Because the inversion procedure is sampling the model space in an efficient way, calculating the misfit between model and observed data, the procedure should be instructed how many iterations are required. Kühn *et al.* (2020) show that 64,000 iterations are required to sample the model effectively. This number is used in our inversion and, for all events, shows conversion to a stable location and moment tensor solution. The inversion package allows the use of many different data attributes in the inversion. Following tests by Kühn *et al.* (2020), we use misfits of seismograms in time-domain, amplitude spectra, and cross-correlations between data and model data. We used all three input data types combined to achieve the best solution. Finally, we invert all events for a full moment tensor to be able to estimate the contribution of the DC, CLVD, and ISO parts of the moment tensor.

In the optimization algorithm of the inversion method, a Bayesian bootstrap method is used (Kühn *et al.*, 2020), resulting in an ensemble of solutions from which the mean and the best solutions are calculated. Similar to the application of the aforementioned inversion technique by Dahm *et al.* (2018), the uncertainty of the inversion results is evaluated by selecting from the database of iteration results the N best from each of the M bootstrap chains, where $N = 10$ and $M = 100$, and thus draw statistics on the 1000 best source models. Our optimization is based on the bootstrap methods of Rubin (1981) and Efron (1979), which is not affected by known pitfalls due to inadequate sampling of the model space. This is because each one of the bootstrap chains converges to a different random point in model space. If the solution distribution has a long tail, a few models far away from the mean have an impact on the standard deviation and can lead to an underestimate of the standard deviation. However, in cases where, for example, the bootstrap configurations may represent bad azimuthal coverage, due to down weighting of stations at one side of the event, these chains are rather unstable, leading to larger scatter. Ideally, at the end of the optimization, the scatter of the best models within each bootstrap chain (intrachain scatter) should have converged below the standard deviation of the best models across all bootstrap chains (interchain scatter). The intrachain scatter would converge to a point, given infinite iterations (but each chain to different point). Taking the 10 best models of each bootstrap chain ensures that any remaining intra-chain (local instabilities, etc.) scatter is accounted for in the solution uncertainties. We tested that adding more iterations to the optimization does not significantly change the estimated uncertainties.

Uncertainty in depth is calculated as the standard deviation over the 1000 best source models. As a measure of uncertainty in the epicenter location, we calculated the distance between the final solution and each of the best solutions in latitude and longitude. This dataset was used to calculate the best-fitting ellipse to the data, characterized by the length of both axes and the rotation angle. The algorithm used to calculate the best-fitting ellipse is described by Fitzgibbon *et al.* (1999). For uncertainty in the moment tensor solution, we calculated the Kagan angle between final and the best source models for the DC solutions, which constitutes the smallest angle to rotate the principal axes of one DC solution to the principal axes of another DC solution (Kagan, 1991). Subsequently, uncertainty

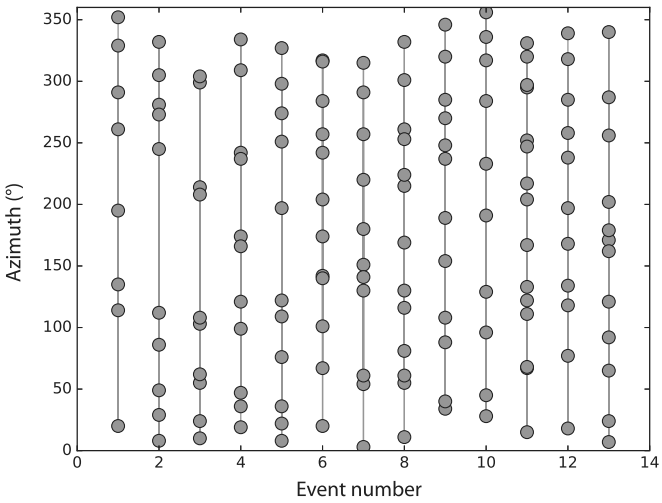

Figure 3. Overview of stations and their azimuth, the data of which are used in the moment tensor inversion. Event numbers correspond to the numbers in Table 1.

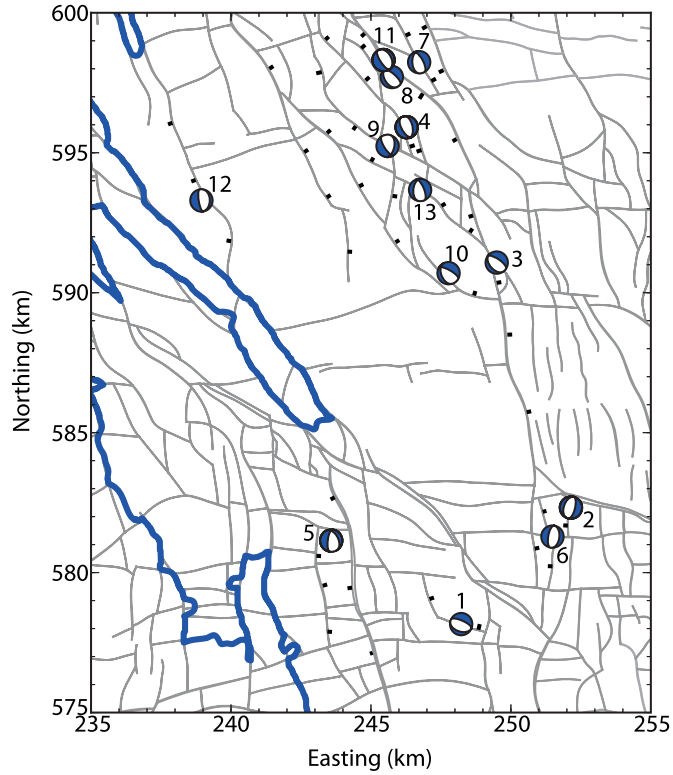

Figure 4. Double-couple (DC) solutions for events listed in Table 1 located in the northwest part of the Groningen gas field. The reservoir fault model is shown in gray, dip direction marked in black (source: Nederlandse Aardolie Maatschappij [NAM], 2016), and field boundary in blue. Event numbers correspond to the numbering in Tables 1 and 2. The selected area is shown in the map in Figure 2. Coordinates are in a local Cartesian system in kilometers (Amersfoort/RD New).

of the DC, ISO, and CLVD component is calculated based on statistics of the Kagan angle for the DC component, and of the percentages of the ISO and CLVD components.

FAULT IDENTIFICATION AND FAULT CHARACTERIZATION

Fault identification and interpretation for the Groningen gas field were based on reprocessed depth-imaged 3D prestack depth migrated (pre-SDM) and reverse-time migrated seismic datasets from 2015 (NAM, 2016). For seismic attribute extractions, including "ant tracking," Petrel software (Schlumberger) was used. Ant tracking is a technology that performs edge enhancement to identify faults within a seismic volume. The moment tensor locations have been plotted on the ant-tracking attribute extraction at top RO depth (Kortekaas and Jaarsma, 2017) to identify the associated faults in map view. Subsequently, these associated faults were interpreted on vertical seismic sections by visual inspection and manual picking. The fault interpretation, defined by fault sticks, was converted to fault-plane interpretations. The fault-plane characteristics mean dip, strike, and vertical offset were determined and compared to the moment tensor inversion solutions.

RESULTS

For the period January 2016 to August 2019, all events of $\mathbf{M} \geq 2.0$ were selected for a moment tensor inversion. In this period, the network density was sufficient to allow for at least four borehole stations to be situated at a maximum distance of 8 km from the epicenter. The selection of larger events assures an acceptable signal-to-noise ratio and prevents that non-DC components could be introduced as artifacts due to inaccurate modeling (e.g., Pesicek *et al.*, 2016). Figure 3 shows, for each event, the number of stations used in the inversion and the azimuthal coverage.

In Tables 1 and 2, results of the inversion are presented, whereas, in Figure 4, results are plotted on top of the NAM fault model (NAM, 2016). In general, the DC solutions show a dominant normal faulting along existing steep (60°–70°) dipping faults at RO reservoir level. Because many faults are present in the reservoir, an evaluation of the accuracy of the hypocenter locations is required before conclusions can be drawn on the connection between events and reactivated existing faults.

Accuracy of hypocenter locations and moment tensor solutions

The depth of almost all hypocenter solutions falls within the depth range of the reservoir derived from the 3D model, when we take their uncertainties into account. Exceptions are events 1 and 5, which show a consistently larger depth below the RO, in the Carboniferous. Both events are located in the southern

TABLE 1
Hypocenter Location and Source Mechanism of Events with M ≥ 2.0 for the Period January 2016 to July 2019

Event Number	Date (yyyy/mm/dd)	M_L	Latitude (°)	Longitude (°)	X_rd	Y_rd	Depth	Strike (°)	Dip (°)	Rake (°)	%ISO	%CLVD
1	2016/02/25	2.4	53.1819	6.7814	248,203	578,149	3040 ± 43	294	62	−86	−42 ± 2	17 ± 8
2	2016/09/02	2.1	53.2201	6.8411	252,108	582,478	2905 ± 103	9	53	−95	−29 ± 4	−6 ± 20
3	2016/11/01	2.2	53.2978	6.8045	249,493	591,076	3000 ± 32	304	60	−98	−27 ± 3	7 ± 6
4	2017/03/11	2.1	53.3418	6.7576	246,274	595,912	3023 ± 24	151	49	−101	−21 ± 3	0 ± 9
5	2017/04/26	2.0	53.2100	6.7126	243,547	581,189	3286 ± 7	187	61	−72	−23 ± 14	−28 ± 15
6	2017/05/27	2.6	53.2092	6.8331	251,598	581,255	2935 ± 78	187	59	−90	−12 ± 6	10 ± 13
7	2017/12/10	2.1	53.3622	6.7666	246,829	598,193	2984 ± 47	330	58	−106	−29 ± 5	7 ± 10
8	2018/01/08	3.4	53.3573	6.7517	245,848	597,629	3030 ± 89	315	62	−95	−29 ± 6	9 ± 10
9	2018/02/08	2.0	53.3359	6.7472	245,593	595,242	2947 ± 20	148	63	−114	−40 ± 2	−13 ± 6
10	2018/02/11	2.2	53.2947	6.7786	247,773	590,697	3004 ± 24	300	65	−108	−27 ± 3	21 ± 9
11	2018/04/13	2.8	53.3635	6.7459	245,449	598,312	3014 ± 28	147	64	−92	−50 ± 2	−6 ± 6
12	2019/05/22	3.4	53.3195	6.6467	238,931	593,295	2953 ± 94	172	67	−95	−15 ± 6	17 ± 18
13	2019/06/09	2.5	53.3221	6.7643	246,762	593,728	3021 ± 40	339	59	−104	−31 ± 4	−10 ± 6

The columns X_rd and Y_rd list coordinates in a local Cartesian system in meters (Amersfoort/RD New).

TABLE 2
Overview of Uncertainty Ellipses for the Epicenters of the Inverted Events, Kagan Angle, and Fault Throw of Reactivated Faults

Event Number	Date (yyyy/mm/dd)	M_L	Major Axis (m)	Minor Axis (m)	Rotation Axis (°)	Average Distance (m)	Average Kagan Angle (°)	Fault Throw (m)
1	2016/02/25	2.4	201	115	102	148 ± 82	16 ± 7	51
2	2016/09/02	2.1	373	208	7	250 ± 166	8 ± 5	30
3	2016/11/01	2.2	177	105	42	138 ± 55	3 ± 2	6
4	2017/03/11	2.1	267	170	133	195 ± 114	8 ± 3	6
5	2017/04/26	2.0	330	139	29	250 ± 119	9 ± 4	13
6	2017/05/27	2.6	216	122	86	150 ± 84	7 ± 4	11
7	2017/12/10	2.1	152	115	53	119 ± 62	7 ± 6	42
8	2018/01/08	3.4	170	105	28	119 ± 74	9 ± 3	60
9	2018/02/08	2.0	251	129	164	157 ± 65	5 ± 2	135
10	2018/02/11	2.2	255	93	129	113 ± 104	6 ± 3	25
11	2018/04/13	2.8	97	91	6	85 ± 47	6 ± 2	163
12	2019/05/22	3.4	174	136	103	134 ± 75	6 ± 3	26
13	2019/06/09	2.5	182	115	115	135 ± 65	4 ± 2	66

Uncertainty ellipses are parameterized with their main axes lengths and rotation angles of the major axes with respect to north. In addition, the average lateral distance and Kagan angle between the mean solution and the best solutions are given. The last column specifies the fault throw of the nearest fault compatible with results from the moment tensor inversions.

part of the Groningen field, where the free water level is located within the underlying Carboniferous. As the gas column continues into the underlying Carboniferous, depletion of the Carboniferous rocks could initiate events within the Carboniferous as well. The fault interpretation of the available reprocessed 3D seismic volumes for the Groningen gas field shows that most faults extend into the Upper Carboniferous strata. For some events, depth resolution is limited due to the fact that in the best solutions two preferred depth ranges show up. Although depth uncertainty derived from the best models is on average small (<50 m), small differences in the velocity models used could easily result in a larger uncertainty around 100 m. Therefore, we assumed a minimum depth uncertainty of 100 m.

Concerning the accuracy of the epicenters, we observe that the direction of the longest axis of the uncertainty ellipse follows the strike of the closest known fault for events 1, 2, 4, 5, 9, and 10 (column 6, Table 2). This means that, for these events, the connection to the nearby fault from the reservoir fault model (NAM, 2016) may be well established, but the position along the fault is less resolved. Other events (3, 6, 7, and 8) do show the direction of the longest axis of the uncertainty ellipse perpendicular to the strike of the faults of the NAM reservoir fault model. Possibly, the more detailed fault model from Kortekaas and Jaarsma (2017) can resolve the associated fault characteristics for these events. Figure 5 shows an example of the uncertainty in the location and moment tensor solutions. The average distance between the result ensemble of all final

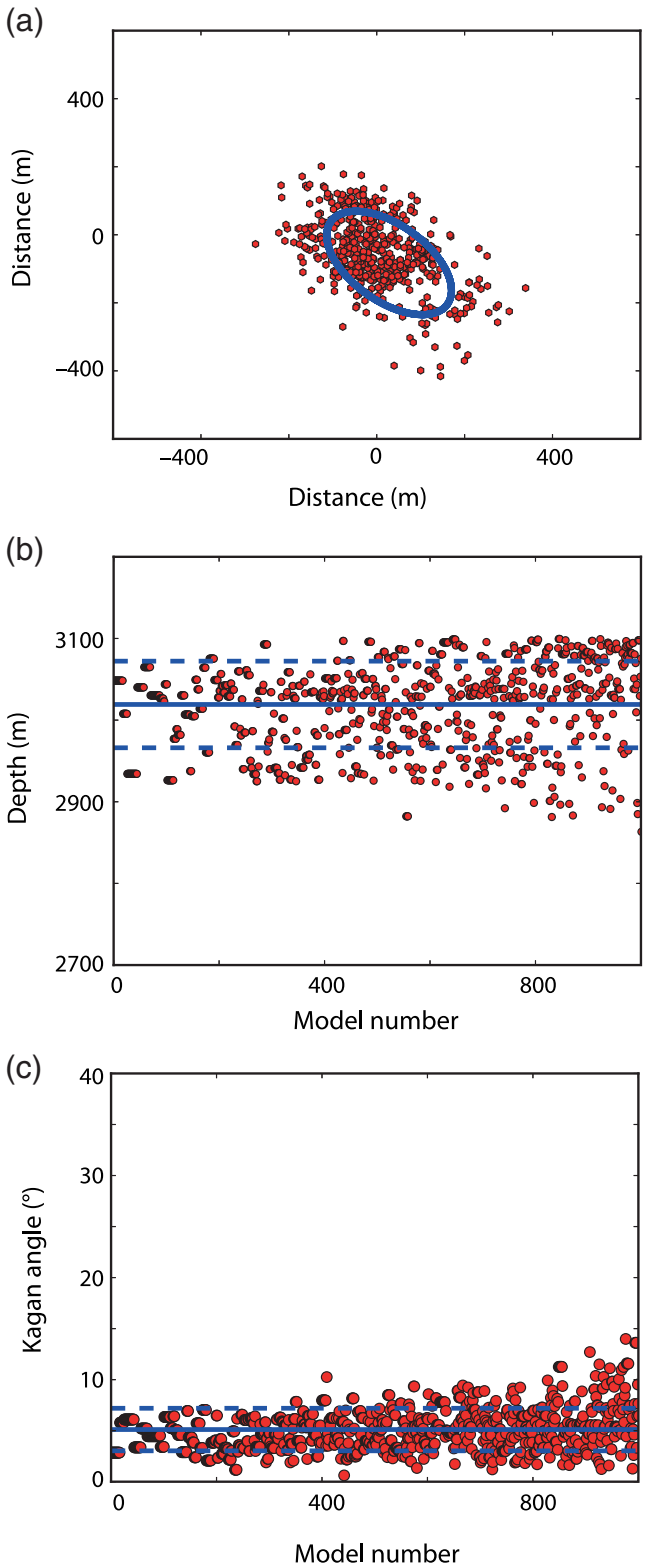

Figure 5. Display of the best 1000 solutions for event 12. (a) Best-fitting ellipse describing the distribution of epicenters, (b) depth distribution with mean (blue line) and 68% confidence zone (dashed line), and (c) development of Kagan angles.

hypocenter solutions and the respective best model is around 160 m, whereas the accuracy of the position of the faults is approximately 100 m (NAM, C. Visser, personal comm., 2019). Finally, the minimum distance between the faults in Figure 4, and the hypocenters of the events in Table 1 is calculated. These distances are, for the most events, smaller than 150 m, so we may conclude that for these events a preliminary connection with existing faults from the reservoir model (NAM, 2016) can be made based on the hypocenter locations. In the following, we will use the more detailed fault model by Kortekaas and Jaarsma (2017) to analyze compatibility of moment tensor solutions and fault geometries.

Comparison with results from other studies

In Figure 6, the epicenter locations for the events in Table 1 are compared to results from full-waveform inversion (Willacy *et al.*, 2018, 2019) and from inversion using the EDT method combined with raytracing in a 3D velocity model (Spetzler and Dost, in preparation). Willacy *et al.* (2019) only published results for three events in Table 1, while additional information could be found in NAM technical reports. A more complete list of all events for the period January 2015 to December 2018, processed by NAM, was communicated early 2019 (NAM, personal comm., 2019), and this list was used for comparison. Unfortunately, events 5, 12, and 13 are missing in this NAM list. The distance from the hypocenters in Table 2 to the EDT results is 238 ± 132 m and to the event locations of full-waveform inversion by Willacy *et al.* (2019) and NAM is 154 ± 76 m. Thus, application of different methods and models result in similar hypocentral locations within 250 m distance.

Based on the same datasets, the best DC parts of the decomposed moment tensor solutions are compared by calculation of the Kagan angle. Results show, on average, a difference between our and NAM solutions around 10°–20°, with two exceptions (Fig. 6b). The first exception is the NAM solution for event 7 with a strike of 5°, dip of 51°, and rake of −67°, which differs 33° in strike and 37° in rake from our best solution. For event 11, a 15° difference in dip (NAM: 79°) and a 44° difference in rake (NAM: −136°) are found.

Interpretation

In Figure 4, the estimated dip direction of the known faults is indicated in black, based on information from NAM (C. Visser, personal comm., 2019) as well as Kortekaas and Jaarsma (2017). Most solutions fit the known faults in strike. Also, the dip direction is in line with the mapped faults, which is an important independent confirmation of the connection between events and existing faults. In the central part of the gas field, between Northing 590 and Northing 600 Rijks-Driehoek (RD) units, the density of events is high. Nevertheless, a clear distinction can be made between reactivated fault segments. Events 8 and 11 are located within 1 km from each other, but these events are located on different faults, dipping in opposite directions (e.g., NAM, 2018).

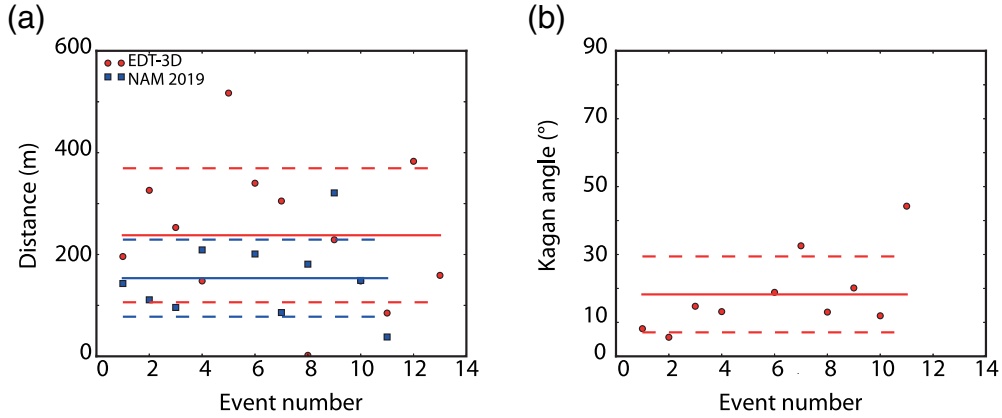

Figure 6. For each event analyzed in this study, we show in (a) the distance between the calculated epicenter location and results from two other studies: equal differential time (EDT)-3D locations in red and Willacy *et al.* (2019) and NAM (personal comm., 2019) in blue, and in (b) the difference between DC parts of moment tensor solutions expressed as the Kagan angle between results from this study and results from NAM (personal comm., 2019). The solid line denotes the mean difference over all events. The dotted line bounds are +1 and −1 standard deviation from the mean.

Kortekaas and Jaarsma (2017) show that fault imaging in the RO and below can be improved significantly using seismic attribute extraction. The fault map based on seismic attributes suggests the presence of faults that have not been included in studies on Groningen seismicity before. Fault interpretation of the reprocessed seismic datasets demonstrates that faults extend from the RO reservoir into the underlying Upper Carboniferous strata. Many faults extend even deeper into the Lower Carboniferous. These datasets allow for a detailed comparison of the fault characteristics with event location and moment tensor.

Seismic sections and map views for all events in Table 1 are available in the supplemental material to this article. Figure 7 shows an example of an association between interpreted faults and results from the moment tensor inversion. A few events are probably located on faults not incorporated in the NAM reservoir model. For these, ant-tracking and manual interpretation were performed to identify the fault characteristics. Event 2 (Fig. S3) is located in between two small faults and on the seismic section perpendicular to the structures; a small reverse fault is visible with strike similar to the moment tensor solution. The hypocenter of event 3 (Fig. S4) is located at a point where two faults merge. Both faults were interpreted and their strike, dip, and offset determined. Based on the moment tensor solution, we assign the event to the fault with the strike angle closest to the moment tensor solution. Event 5 (Fig. S6) is located between two faults of the NAM reservoir fault model, with the nearest fault at 400 m distance. A small additional fault could be identified in the seismic sections, which is compatible with strike and dip from the moment tensor inversion. Event 6 (Fig. S7) is located at a site where three faults join each other. The major east–west fault has a strike perpendicular to the moment tensor solution and is most likely not associated with this event. Instead, a small north–south oriented fault, visible within the reservoir in the seismic section and on the ant-tracking attribute extraction at top RO, is likely associated to this event. The hypocenter of event 8 (Fig. 7) with magnitude $\mathbf{M}_L$ 3.4 is located between two faults. Based on the moment tensor solution, the associated fault is most likely the cyan dashed fault with only a small vertical offset. Buijze *et al.* (2017) discuss the importance of the existence of a fault throw on the timing and location of seismic slip due to reactivation of the fault and also on the rupture size. A comparison of event locations with published fault throw maps, for example, Lele *et al.* (2015) and de Zeeuw *et al.* (2018), demonstrates that with the exception of events 9 and 11, all other events in Table 1 occur along faults characterized by a relatively small throw (<70 m).

Non-DC components

Both our solutions and NAM solutions specify the percentage of non-DC components in the solution, as ISO component and CLVD. In the present study, percentages are calculated following Vavrycuk (2001). Before the end of 2017, the non-DC contributions are small (<10%) in the NAM solutions, whereas this percentage increases for more recent events, due to a relaxation of the constraints in their procedures (Van Dedem, personal comm., 2019; Willacy *et al.*, 2019). In our inversion (Table 1), all percentages of ISO components are negative, indicating a decreasing volume, which should be expected in a compacting medium. Especially for event 11, the absolute value of the ISO component is high (50% Royal Netherlands Meteorological Institute, 60% NAM). To analyze this event, it is essential to employ a full moment tensor inversion, because inversions restricted to a deviatoric moment tensor do not provide a solution that can be interpreted in terms of the local fault system. In Figure 8, we show the waveform fits for the *P* wave for the inversion results for event 11. The full moment tensor inversion results show a large ISO and DC component, and nearly no CLVD component (Fig. 8a). The waveform fits are, in general, very good. Figure 8b shows results for inversion where we only invert for the deviatoric component. This results in a large CLVD component and a very small DC component. The waveform fits are reasonable in some stations, but very

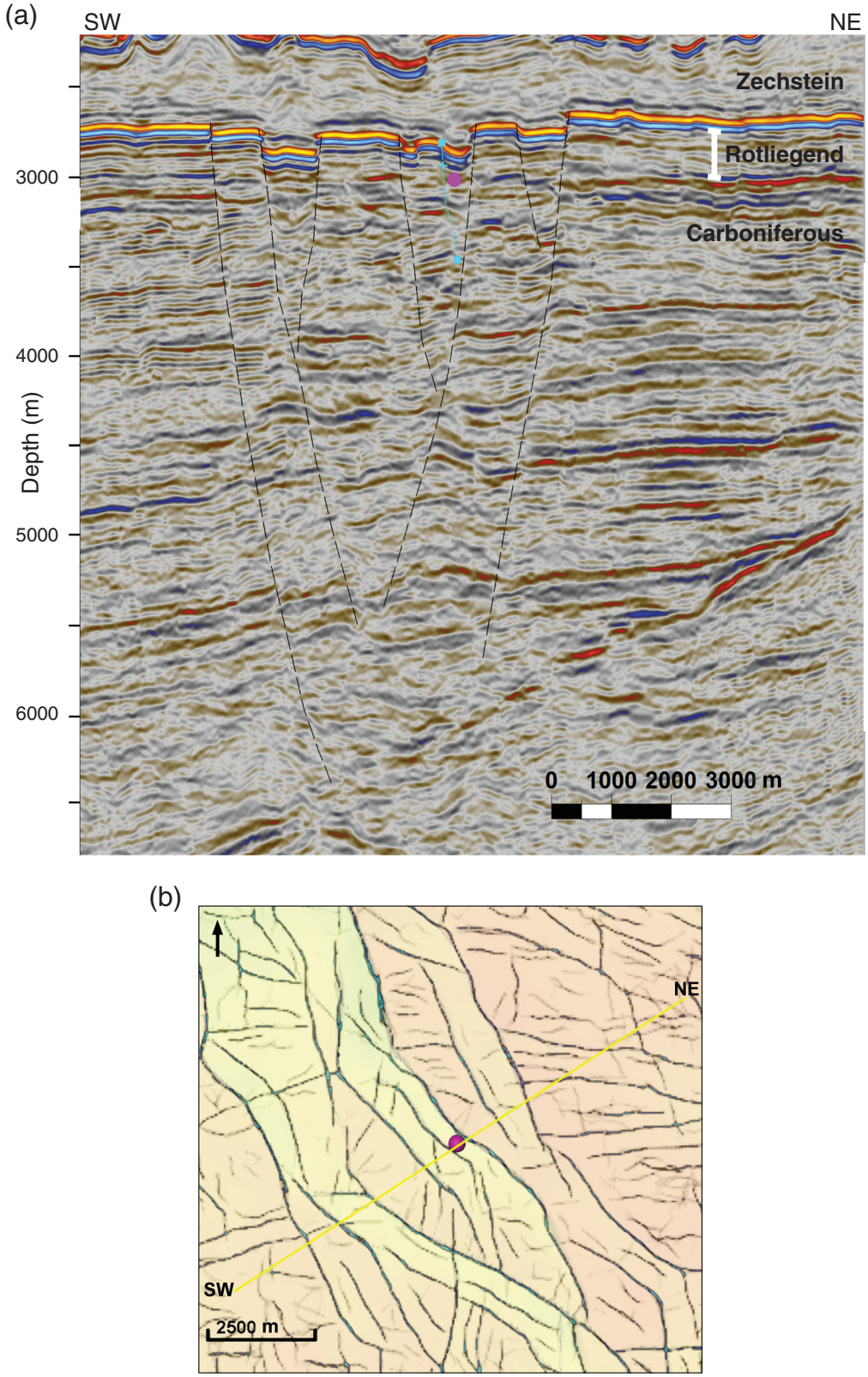

Figure 7. (a) Southwest (SW)–northeast (NE) seismic section, displaying the deep-seated fault interpretation (black dashed lines). The location of the section is indicated by the yellow line in panel (b). The hypocenter of event 8 is marked by a purple circle. Its location in the gas field is shown in Figure 4. The cyan dashed line indicates the interpreted fault associated with the hypocenter of event 8. (b) Seismic attribute extraction at top reservoir indicating the presence of faults (dark lines) and event location (purple circle).

poor in others. The inversion procedure was unable to find a good solution. In an ideal situation, when the complete radiation pattern of the source (above and below) is fully captured by the recording stations, a trade-off between CLVD and ISO components is not expected. In practice, however, this trade-off is more often observed. One example is the analysis of the 2016 nuclear explosion in North Korea (Cesca *et al.*, 2017), where trade-offs among horizontal and vertical Moment Tensor dipoles are found responsible for the trade-off among ISO and CLVD terms. The fact that the NAM solution is close to our solution, using a different method and the full 3D model, gives us additional assurance that the high ISO component is a real feature and not influenced by the choice of a 1D velocity model. The CLVD percentage is, on average, lower than the ISO percentage and has a larger uncertainty. This can be seen in Figure 9, where percentages are plotted including their uncertainty. It is worth noting that both events associated with a fault exhibiting a larger throw show the highest percentage of the ISO component.

Vavrycuk (2001, 2015) discusses the physical properties of the decomposition of the full moment tensor. For nonzero ISO and CLVD components, a shear-tensile source is the only possible interpretation, and, for negative ISO and CLVD components, this implies a compressive mechanism. A requirement for tensile faulting, however, is a positive ISO/CLVD ratio, and this is often not the case for our

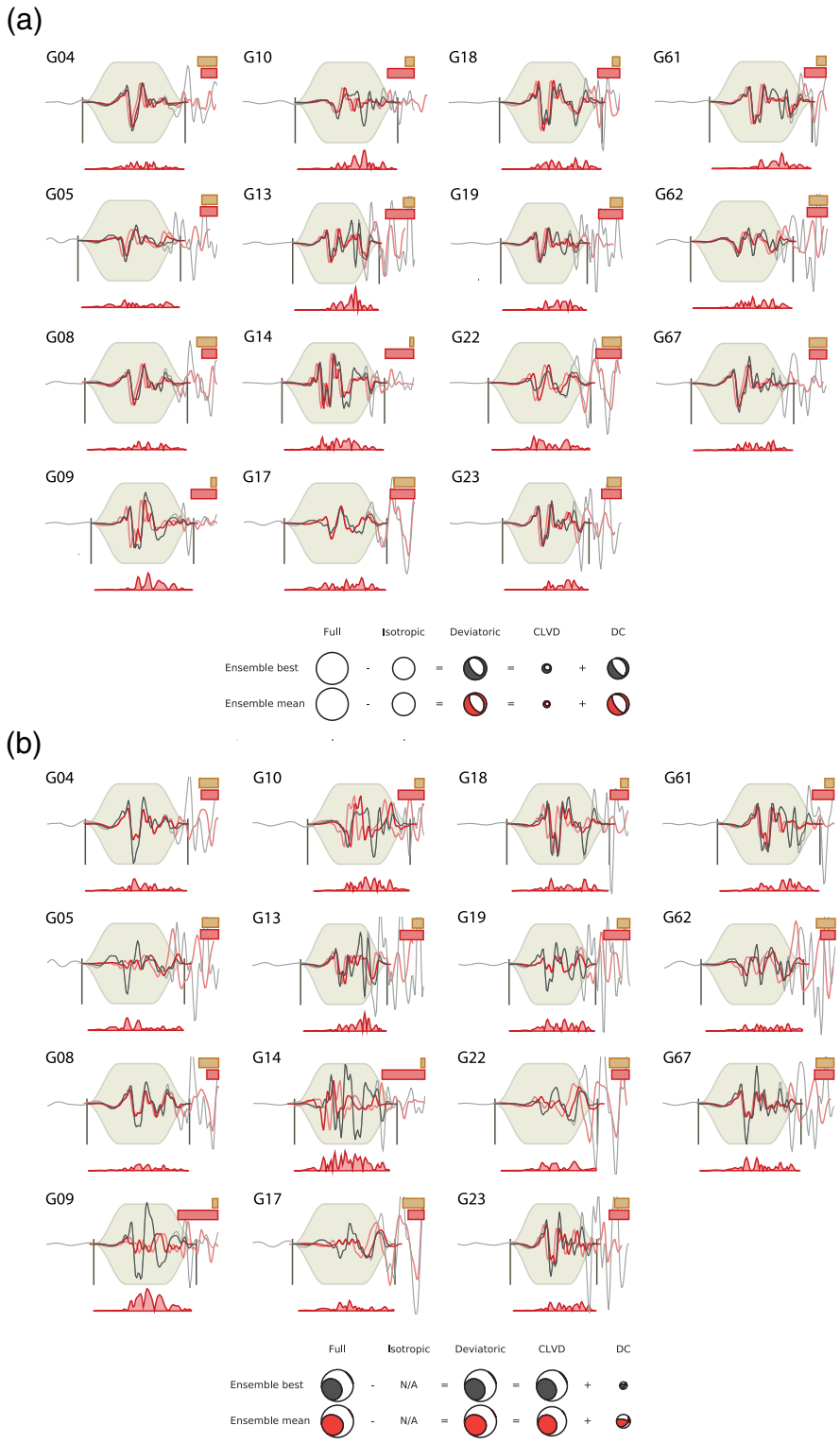

Figure 8. Overview of observed (black) and synthetic waveforms (red) of the *P* waves from event 11 (Table 1). (a) Waveform fits for the full moment tensor inversion and (b) the inversion for the deviatoric component. Light colors indicate tapered and strong colors untapered data; whereas light red traces are unshifted in time, dark red traces are final fits. Residuals are shown at the bottom of each station panel as a red distribution. Relative weighting factors and residuals are indicated by yellow and red bars, respectively. Station name is indicated at the top left of the individual waveform panels. All waveforms have been recorded at 150 m depth. The vertical gray bars indicate the onset time (left) and end time (right) of the waveform interval. All intervals have a duration of 3.2 s. The colored background shows the taper window. At the bottom of the waveform panels, the best and mean moment tensor solutions are displayed. CLVD, compensated linear vector dipole.

results. This could be due to uncertainties in the ratio calculations, resulting from either an inaccurate velocity model or a more complicated source model. If we assume that the events with a positive ratio can be interpreted as tensile sources, we can calculate the inclination of the slip vector. For events 5, 9, 11, and 13, the angle is small, that is, −17°, −10°, −5°, and −3°, respectively. In an earlier article, Vavrycuk (2005) discusses the influence of anisotropy in the source region on the non-DC part of the moment tensor. Romijn (2017) provides information on anisotropy in the velocity model for Groningen and concluded that from interpretation of pre-SDM data weak anisotropy is detected in the layers above the thick ZE formation was found and no anisotropy in the RO reservoir where all seismicity was located. Therefore, we do not expect influence of anisotropy in our results.

Cesca *et al.* (2013) found similar results of a negative ISO/CLVD ratio in the analysis of an induced event near Teutschenthal in 1996, where an implosive ISO component was found together with a positive CLVD component. The authors showed that an alternative decomposition of the deviatoric term into a superposition of a normal fault and a positive CLVD component can explain the findings. A similar decomposition for Groningen showed comparable results.

CONCLUSION

Full moment tensor inversion combined with an improved location accuracy of induced

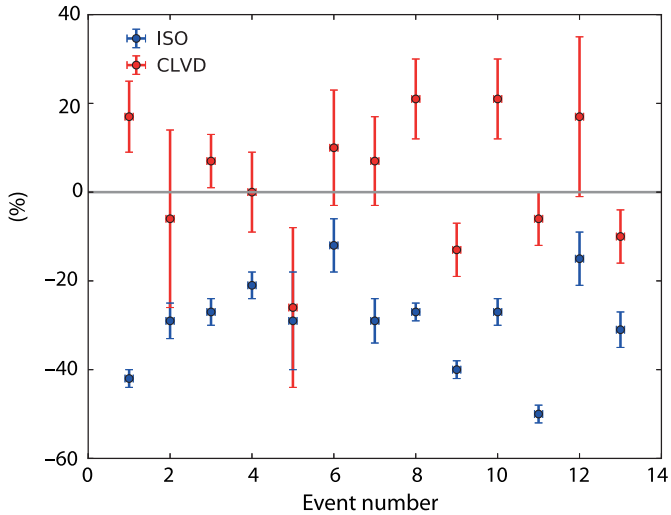

Figure 9. Percentages of isotropic (ISO) and CLVD components for events listed in Table 1. Squares denote mean values, whereas the error bars depict the range between +1 and −1 standard deviation from the mean.

events provides new insight in the process of reactivation of existing faults within the Groningen gas field. The seismic attribute extraction and fault interpretation of the reprocessed 3D seismic volumes of the Groningen gas field result in a detailed fault model and the identification of deep-seated faults. We show that the moment tensor solutions generally correspond well to the fault characteristics. Although most hypocenters are limited to the reservoir level around 3 km depth, some events potentially indicate a deeper origin.

DATA AND RESOURCES

The seismic waveform data used in the inversion are publicly available from the Royal Netherlands Meteorological Institute (KNMI) portal at http://rdsa.knmi.nl/dataportal (last accessed September 2019). The Python-based inversion code Grond and its description can be found at https://pyrocko.org/grond/ (last accessed August 2018). Green's functions databases were computed with the Python Pyrocko-GF software library residing at https://pyrocko.org/ (last accessed August 2018). The python implementation of the algorithm to calculate the best-fitting ellipse to a data cloud can be found at http://nicky.vanforeest.com/misc/fitEllipse/fitEllipse.html (last accessed January 2020). A small correction to the published code was required (within the fitEllipse routine, the absolute value of parameter E should be removed: np.abs (E) -> E). The 3D pre-stack depth-migrated and reverse-time-migrated seismic datasets were provided by Nederlandse Aardolie Maatschappij (NAM) and are proprietary. They cannot be released to the public. This article includes the supplemental material that shows the association with reinterpreted seismic sections for each earthquake listed in Table 1.

ACKNOWLEDGMENTS

The authors thank Marius Isken (University of Kiel, Germany) for his assistance in the set-up and usage of the Grond/Pyrocko software. In addition, the authors are grateful to the Nederlandse Aardolie Maatschappij (NAM) for sharing their moment tensor inversion results, discussions on the subject, and permission to show images of the prestack depth-migrated 2015 Groningen dataset. Finally, the authors thank the editors and two anonymous reviewers for their constructive comments.

REFERENCES

Bourne, S. J., S. J. Oates, J. van Elk, and D. Doornhof (2014). A seismological model for earthquakes induced by fluid extraction from a subsurface reservoir, *J. Geophys. Res.* **119,** 8991–9015, doi: 10.1002/2014JB011663.

Buijze, L., P. A. J. van den Bogert, B. B. T. Wassing, B. Orlic, and J. ten Veen (2017). Fault reactivation mechanics and dynamic rupture modelling of depletion-induced seismic events in a Rotliegend gas reservoir, *Netherlands J. Geosci.* **96,** s131–s148, doi: 10.1017/njg.2017.27.

Cesca, S., S. Heimann, M. Kriegerowski, J. Saul, and T. Dahm (2017). Moment Tensor Inversion for Nuclear Explosions: What can we learn from the 6 January and 9 September 2016 Nuclear Tests, North Korea?, *Seismol. Res. Lett.* **88,** no. 2A, 300–310.

Cesca, S., A. Rohr, and T. Dahm (2013). Discrimination of induced seismicity by full moment tensor inversion and decomposition, *J. Seismol.* **17,** 147–163, doi:10.1007/s10950-012-9305-8.

Dahm, T., S. Heimann, S. Funke, S. Wendt, I. Rappsilber, D. Bindi, T. Plenefisch, and F. Cotton (2018). Seismicity in the block mountains between Halle and Leipzig, Central Germany: Centroid moment tensors, ground motion simulation, and felt intensities of two $M \approx 3$ earthquakes in 2015 and 2017, *J. Seismol.* **22,** 985–1003, doi: 10.1007/s10950-018-9746-9.

Daniel, G., E. Fortier, R. Romijn, and S. Oates (2016). Location results from borehole microseismic monitoring in the Groningen gas reservoir, Netherlands, *Sixth EAGE Workshop on Passive Seismic, Extended abstract*, doi: 10.3997/2214-4609.201600016.

De Jager, J., and C. Visser (2017). Geology of the Groningen field – an overview, *Netherlands J. Geosci.* **96,** s3–s15, doi: 10.1017/njg.2017.22.

De Zeeuw, Q., and L. Geurtsen (2018). Groningen Dynamic Model Update 2018, *NAM report*, available at http://feitenencijfers.namplatform.nl/onderzoeksrapporten/ (last accessed February 2019).

Dost, B., and H. Haak (2007). Natural and induced seismicity, in *Geology of the Netherlands*, T. E. Wong, D. A. J. Batjes, and J. de Jager (Editors), Royal Netherlands Academy of Arts and Sciences, Amsterdam, The Netherlands, 223–239.

Dost, B., E. Ruigrok, and J. Spetzler (2017). Development of seismicity and probabilistic hazard assessment for the Groningen gas field, *Netherlands J. Geosci.* **96,** s235–s245, doi: 10.1017/njg.2017.20.

Efron, B. (1979). Bootstrap methods: Another look at the jackknife, *Ann. Stat.* **7,** 1–26.

Fitzgibbon, A., M. Pilu, and R. B. Fisher (1999). Direct least square fitting of ellipses, *IEEE Trans. Pattern Anal. Mach. Intell.* **21,** 476–480.

Fletcher, J. B., and A. McGarr (2005). Moment tensor inversion of ground motion from mining-induced earthquakes, trail mountain, Utah, *Bull. Seismol. Soc. Am.* **95,** 48–57, doi: 10.1785/0120040047.

Gu, C., Y. M. Marzouk, and M. N. Toksöz (2018). Waveform-based Bayesian full moment tensor inversion and uncertainty determination for the induced seismicity in an oil/gas field, *Geophys. J. Int.* **212,** 1963–1985, doi: 10.1093/gji/ggx517.

Heimann, S., M. Kriegerowski, M. Isken, S. Cesca, S. Daout, F. Grigoli, C. Juretzek, T. Megies, H. Nooshiri, A. Steinberg, *et al.* (2017). *Pyrocko – An Open Source Seismology Toolbox and Library, V. 0.3*, GFZ Data Services, doi: 10.5880/GFZ.2.1.2017.001.

Hofman, L. J., E. Ruigrok, B. Dost, and H. Paulssen (2017). A shallow seismic velocity model for the Groningen area in the Netherlands, *J. Geophys. Res.* **122,** 8035–8050, doi: 10.1002/2017JB014419.

Julià, J., A. A. Nyblade, R. Durrheim, L. Linzer, R. Gök, P. Dirks, and W. Walter (2009). Source mechanisms of mine-related seismicity, Savuka mine, South Africa, *Bull. Seismol. Soc. Am.* **99,** 2801–2814, doi: 10.1785/0120080334.

Kagan, Y. Y. (1991). 3-D rotation of double-couple earthquake sources, *Geophys. J. Int.* **106,** 709–716.

Kortekaas, M., and B. Jaarsma (2017). Improved definition of faults in the Groningen field using seismic attributes, *Netherlands J. Geosci.* **96,** s71–s85, doi: 10.1017/njg.2017.24.

Kraaijpoel, D., and B. Dost (2013). Implications of salt-related propagation and mode conversion effects on the analysis of induced seismicity, *J. Seismol.* **17,** 95–107.

Kühn, D., S. Heimann, M. Isken, E. Ruigrok, and B. Dost (2020). Probabilistic moment tensor estimation for hydrocarbon-induced seismicity in the Groningen gas field, the Netherlands, part 1: Testing, *Bull. Seismol. Soc. Am.* doi: 10.1785/0120200099.

Kühn, D., and V. Vavryčuk (2013). Determination of full moment tensors of microseismic events in a very heterogeneous mining environment, *Tectonophysics* **589,** 33–43.

Lele, S. P., J. L. Garzon, S.-Y. Hsu, N. L. DeDontney, K. H. Searles, P. F. Sanz, and , and ExxonMobil Upstream Research Company, Spring TX, and Groningen (2015). Geomechanical analysis, *NAM report*, available at http://feitenencijfers.namplatform.nl/onderzoeksrapporten/ (last accessed February 2019).

Li, J., H. Kuehl, A. Droujinine, and J.-W. Blokland (2016). Microseismic and induced seismicity simultaneous location and moment tensor inversion: Moving beyond picks with a robust full waveform method, *SEG Technical Program Expanded Abstracts*, 2535–2539.

Lomax, A. (2005). A Reanalysis of the hypocentral location and related observations for the Great 1906 California earthquake, *Bull. Seismol. Soc. Am.* **95,** 861–877.

Martínez-Garzón, P., G. Kwiatek, M. Bohnhoff, and G. Dresen (2017). Volumetric components in the earthquake source related to fluid injection and stress state, *Geophys. Res. Lett.* **44,** 800–809, doi: 10.1002/2016GL071963.

McGarr, A. (1992). An implosive component in the seismic moment tensor of a mining-induced tremor, *Geophys. Res. Lett.* **19,** 1579–1582.

Nederlandse Aardolie Maatschappij (NAM) (2016). *Technical Addendum to the Winningsplan Groningen 2016 – Production, Subsidence, Induced Earthquakes and Seismic Hazard and Risk Assessment in the Groningen Field, Part 1*, van Elk, J. and D. Doornhof (Editors), Nederlandse Aardolie Maatschappij, Assen, The Netherlands.

NAM (2018). *Special Report on the Zeerijp Earthquake – 8th January 2018*, den Bezemer, T. and J. van Elk (Editors), Nederlandse Aardolie Maatschappij, Assen, The Netherlands.

Noorlandt, R., P. P. Kruiver, M. P. de Kleine, M. Karaoulis, G. de Lange, A. Di Matteo, and J. J. Bommer (2018). Characterisation of ground motion recording stations in the Groningen gas field, *J. Seismol.* **22,** no. 3, 605–623.

Pesicek, J. D., K. Cieslik, M.-A. Lambert, P. Carrillo, and B. Birkelo (2016). Dense surface seismic data confirm non-double couple source mechanisms induced by hydraulic fracturing, *Geophysics* **81,** KS207–KS217.

Pickering, M. (2015). An estimate of the earthquake hypocenter locations in the Groningen gas field, *NAM report*, available at http://feitenencijfers.namplatform.nl/onderzoeksrapporten/ (last accessed February 2019).

Romijn, R. (2017). *Groningen velocity model 2017 – Groningen full elastic velocity model*, *NAM report*, 12 pp.

Rubin, D. B. (1981) The Bayesian bootstrap, *Ann. Stat.* **9,** 130–134.

Ruigrok, E., J. Domingo-Ballesta, G-J. van den Hazel, B. Dost, and L. Evers (2019). Groningen explosion database, *First Break* **37,** 37–41.

Spetzler, J., and B. Dost (2017). Hypocenter estimation of induced earthquakes in Groningen, *Geophys. J. Int.* **209,** 453–465, doi: 10.1093/gji/ggx020.

Tan, Y., H. Zhang, J. Li, C. Yin, and F. Wu (2018). Focal mechanism determination for induced seismicity using the neighbourhood algorithm, *Geophys. J. Int.* **214,** 1715–1731, doi: 10.1093/gji/ggy224.

Vavrycuk, V. (2001). Inversion for parameters of tensile earthquakes, *J. Geophys. Res.* **106,** 16339–16355.

Vavrycuk, V. (2005). Focal mechanisms in anisotropic media, *Geophys. J. Int.* **161,** 334–346, doi: 10.1111/j.1365-246X.2005.02585.x.

Vavrycuk, V. (2015). Moment tensor decompositions revisited, *J. Seismol.* **19,** 231–252, doi: 10.1007/s10950-014-9463-y.

Wang, R. (1999). A simple orthonormalization method for stable and efficient computation of Green's functions, *Bull. Seismol. Soc. Am.* **89,** 733–741.

Wang, R., Y. J. Gu, R. Schultz, and Y. Chen (2018). Faults and non-double-couple components for induced earthquakes, *Geophys. Res. Lett.* **45,** 8966–8975, doi: 10.1029/2018GL079027.

Willacy, C., E. van Dedem, S. Minsini, J. Li, J. W. Blokland, I. Das, and A. Droujinine (2018). Application of full-waveform event location and moment-tensor inversion for Groningen induced seismicity, *Leading Edge* **37,** 92–99, doi: 10.1190/tle37020092.1.

Willacy, C., E. van Dedem, S. Minsini, J. Li, J. W. Blokland, I. Das, and A. Droujinine (2019). Full waveform event location and moment tensor inversion for induced seismicity, *Geophysics* **84,** KS39–KS57, doi: 10.1190/GEO2018-0212.1

Zhang, H., D. W. Eaton, G. Li, Y. Liu, and R. M. Harrington (2016). Discriminating induced seismicity from natural earthquakes using moment tensors and source spectra, *J. Geophys. Res.* **121,** 972–993, doi: 10.1002/2015JB012603.

Manuscript received 17 February 2020
Published online 11 August 2020